Catalysis
Science &
Technology

ROYAL SOCIETY
OF CHEMISTRY

PAPER

View Article Online
View Journal | View Issue

Cite this: *Catal. Sci. Technol.*, 2025, **15**, 6059

CO esterification to methyl formate: from Pd nanoparticles to single atom catalysts

Xiao-Long Wang,[ab] Xiao-Yuan Tan,[ab] Jian Lin,[c] Hua Wang,[d] Jing Sun,[b]
Zhong-Ning Xu *[b] and Guo-Cong Guo [b]

CO esterification involves processes using CO as the starting material and ester chemicals as products. Methyl formate, dimethyl oxalate and dimethyl carbonate are the main products. Traditional Pd nanoparticle (Pd_{NP}) catalysts have excellent catalytic performance for the CO esterification reaction. However, Pd_{NP} catalysts have problems such as high metal loading, low metal utilization and high cost. In recent years, single atom catalysts have developed rapidly due to their high atomic utilization and low loading. In this work, $Pd_1/(ZnMn_2O_4@MnO_2)$ (Pd_1/ZMO) was synthesized *via* a sol–gel method followed by a redispersion strategy-assisted calcination process. This Pd_1/ZMO catalyst exhibits exceptional catalytic performance for CO esterification to methyl formate. Compared to the $Pd_{NP}/\alpha\text{-}Al_2O_3$ catalyst, Pd single atom catalysts significantly reduce noble metal loading from 1 wt% to 0.25 wt%, while increasing the catalyst's mass activity by 4 times. More importantly, the Pd_1/ZMO catalyst is quite stable at least for 150 hours under reaction conditions. And we have demonstrated the high dispersibility of the Pd single atom through AC-TEM, *in situ* DRIFTS and XPS. This work adopts the strategy of single atom catalyst, which controls the cost of the catalyst while achieving a 4-fold increase in metal utilization, providing important reference significance for the efficient utilization of noble metal and catalyst cost control.

Received 10th July 2025,
Accepted 14th August 2025

DOI: 10.1039/d5cy00841g

rsc.li/catalysis

1. Introduction

CO stands out as one of the most versatile and cost-effective gases derived from natural gas, coal, and biomass. Given the rapid depletion of petroleum and coal resources, coupled with the imperative to advance carbon neutrality principles, the catalytic esterification of CO into high-value-added chemicals has gained increasing significance. The CO esterification reaction serves as a critical bridge between C1 chemistry and premium ester products, with its enhanced catalytic efficiency holding strategic importance for the chemical, energy, and environmental sectors.[1] As the simplest ester in C1 chemistry, methyl formate (MF) is of particular value due to its role as a pivotal chemical intermediate.

MF is a significant chemical reagent commonly employed in the production of fungicides, gasoline additives, and pharmaceutical synthesis intermediates.[2] A wide array of industrial chemicals can be derived from MF, including formic acid, formamide and methyl acrylate, among other fine chemicals. Additionally, MF has been identified as an excellent hydrogen storage material due to its non-toxic nature, ease of transportation, and high hydrogen content (8.4 wt%).[3] There are several methods for producing MF, such as liquid-phase methanol carbonylation, one-step syngas synthesis and other methods.[4–8] Among them, liquid-phase methanol carbonylation is the most commonly used method for industrial MF synthesis.

Our research group has developed a new method for CO esterification to MF.[9] Through exploration, we found that Pd-based catalysts have good catalytic activity in CO esterification. We found that the $Pd/\alpha\text{-}Al_2O_3$ catalyst has excellent performance for CO esterification to MF. However, Pd exists in the form of nanoparticles in the catalyst, which leads to a low utilization rate and high cost of noble metals in the catalyst. Single-atom catalysts have emerged as a focal point in recent years, finding widespread applications in various fields such as electrochemistry, photocatalysis, and traditional thermal catalysis. They exhibit outstanding performance and activity in reactions including water–gas conversion,[10] C–C coupling,[11] photocatalytic hydrogen production,[12–14] and methanol reforming.[15] Compared with nanoparticle catalysts, single-atom catalysts have the

---

[a] *College of Chemistry and Materials Science, Fujian Normal University, Fuzhou 350007, P. R. China*
[b] *State Key Laboratory of Structural Chemistry, Fujian Institute of Research on the Structure of Matter, Chinese Academy of Sciences, Fuzhou 350002, P. R. China. E-mail: znxu@fjirsm.ac.cn*
[c] *CAS Key Laboratory of Science and Technology on Applied Catalysis, Dalian Institute of Chemical Physics, Chinese Academy of Sciences, Dalian 116023, P. R. China*
[d] *School of Chemistry and Chemical Engineering, Yulin University, Yulin, Shaanxi 719000, P. R. China*

characteristics of high atomic utilization efficiency and high activity.[16–18]

This study synthesized $Pd_1/(ZnMn_2O_4@MnO_2)$ (denoted as Pd_1/ZMO) *via* a sol–gel method followed by a redispersion strategy-assisted calcination process. The combination of high temperature and strong interactions with the support material leads to the formation of $ZnMn_2O_4@MnO_2$ heterojunctions on the support surface during calcination, thereby enhancing the metal–support interaction.[19–21] Compared to the $Pd_{NP}/\alpha\text{-}Al_2O_3$ catalyst, Pd_1/ZMO reduced Pd loading from 1 wt% to 0.25 wt%, while increasing the catalyst's mass activity by 4 times. At the same time, there was no decrease in the stable performance during the 150-hour reaction. Furthermore, the selectivity for MF reached 96%, with a weight-time yield of 1318 g kg_{cat}^{-1} h^{-1}. Furthermore, by employing *in situ* electron paramagnetic resonance (*in situ* EPR) and diffuse reflectance infrared Fourier transform spectroscopy (*in situ* DRIFTS) analyses, complemented by mechanistic insights from prior studies, we propose a plausible reaction pathway for the CO esterification to MF. Experimental feasibility of scaling up the catalyst for CO esterification to MF from the nanoparticle to single-atom scale further validates the advantages of single-atom catalysts, thereby broadening their application fields.

2. Experiment

2.1. Preparation of catalysts

The Pd_{NP}/ZMO catalyst prepared by the co-precipitation method was as follows: initially, 6.22 g of $Zn(NO_3)_2\cdot 6H_2O$ and 19.76 g of citric acid were dissolved in 100 mL of deionized water. Subsequently, 10 mL of 50% $Mn(NO_3)_2$ solution and 0.6 g of $Pd(NO_3)_2$ were added, and the mixture was stirred at room temperature overnight. The resultant solution was then heated in a water bath at 60 °C until it became viscous and foamy, resulting in a wet gel. This wet gel was dried overnight at 150 °C to obtain a dry gel. Finally, the dry gel was calcined in a muffle furnace at a heating rate of 1 °C min^{-1} up to 500 °C and maintained for 4 h, then heated in a 10% H_2/Ar at a rate of 2 °C min^{-1} to 200 °C and maintained for 2 h, yielding the sample designated as Pd_{NP}/ZMO.

The Pd_1/ZMO catalyst prepared by the co-precipitation method was as follows: the Pd_{NP}/ZMO sample was treated with a prepared 1 M dilute nitric acid solution, stirred for 30 minutes, filtered, and washed several times until the pH of the filtrate approached 7. The precipitate was then dried overnight at 80 °C. Finally, the sample was heated in a muffle furnace at a rate of 1 °C min^{-1} to 350 °C and calcined for 2 h to produce the Pd_1/ZMO catalyst.

The $Pd_{NP}/\alpha\text{-}Al_2O_3$ catalyst was synthesized using the conventional impregnation stirring method.

2.2. Characterization

ICP. The content of loaded Ni was analyzed by inductively coupled plasma (ICP), which was carried out on an Ultima 2 plasma emission spectrometer from Jobin Yvon.

BET. The surface area of the samples was determined by N_2 adsorption–desorption isotherms, performed on a Micromeritics ASAP 2020 at liquid nitrogen temperature (77 K).

XRD. Powder X-ray diffraction (XRD) patterns of the catalyst powders were obtained with a Rigaku Miniflex 600 diffractometer using Cu Kα radiation (λ = 1.5406 Å) with a scan speed of 3° min^{-1} in the range of 5–80°.

XPS. X-ray photoelectron spectroscopy (XPS) was performed on an Escalab 250 spectrometer (VG Systems) equipped with an Al Kα (1486.6 eV) anode as the X-ray source. The binding energies were corrected by the C 1s peak at 284.6 eV, providing experimental errors within ±0.1 eV.

TEM. Transmission electron microscopy (TEM) was performed on a FEI Talos F200x field-emission transmission electron microscope operated at 120 kV.

AC-TEM. Special aberration corrected transmission electron microscope (AC-TEM) was performed on a Talos F200x G2 operated at 200 kV.

NH_3-TPD. The NH_3 temperature-programmed desorption (NH_3-TPD) was performed on a TP-5080. Before each measurement, a 100 mg sample was pretreated at 200 °C for 1 h with the He flow at 30 mL min^{-1} and 10 °C min^{-1}. The adsorption was operated at 50 °C for 30 minutes in 10% NH_3/He flow at 30 mL min^{-1}, followed by He purging for 30 minutes. The NH_3 desorption of the catalyst samples was performed at a heating rate of 10 °C min^{-1} and heating from 30 °C to 700 °C.

Raman. The Raman spectroscopy was performed on a LabRAM HR Evolution confocal Raman micro-spectrometer under ambient conditions. The excitation wavelength of the laser was 633 nm and the measurement range was 1000–2000 cm^{-1}.

EPR. Electron paramagnetic resonance (EPR) was performed on a Bruker E500 spectrometer. About 100 mg of the solid sample was weighed and put into a paramagnetic test tube to test the oxygen vacancy.

***In situ* DRIFTS.** *In situ* diffuse reflectance infrared Fourier transform spectroscopy (*in situ* DRIFTS) was performed on a Nicolet 6700 and the spectra were recorded in the range of 600–4000 cm^{-1} at a resolution of 4 cm^{-1} over 32 scans.

TOF-SIMS. The time-of-flight secondary ion mass spectrometry (TOF-SIMS) was performed on a TOF-SIMS 5–100 instrument by negative ion mode scanning.

2.3. Catalyst evaluation

For each evaluation, a catalyst dosage of 200 mg was used in a fixed-bed reactor, where the reaction gases CO, H_2 and methyl nitrite (MN) were introduced to assess performance. The reaction device is a fixed bed device. The catalyst is filled in a special quartz tube, fixed up and down by quartz cotton, and some quartz sand is filled on the upper quartz cotton. Peak intensities of MN, MF, and CO were analyzed using a Shimadzu gas chromatograph (GC-2014). And the data are collected with a Shimadzu GC-2014 chromatograph.

Catalyst evaluation conditions: catalyst loading 200 mg each time, reaction gas space velocity 3000 h^{-1}, reaction gas pressure 0.1 MPa, reaction gas ratio $CO:MN:H_2 = 1.4:1:0.6$, and evaluation temperature 120 °C.

2.4. Calculation of parameters

The calculation formula is as follows:

$$\text{Conversion of CO (\%)} = ([\mathrm{CO}]_{\mathrm{in}}/[\mathrm{Ar}]_{\mathrm{in}} - [\mathrm{CO}]_{\mathrm{out}}/[\mathrm{Ar}]_{\mathrm{out}})/([\mathrm{CO}]_{\mathrm{in}}/[\mathrm{Ar}]_{\mathrm{in}}) \times 100\%$$

$$\text{Selectivity of MF (\%)} = (A_{\mathrm{MF}} \times R - F_{\mathrm{MF}}/M_{\mathrm{MF}})/(3 \times A_{\mathrm{DMM}} \times R - F_{\mathrm{DMM}}/M_{\mathrm{DMM}} + A_{\mathrm{MF}} \times R - F_{\mathrm{MF}}/M_{\mathrm{MF}} + 2 \times A_{\mathrm{DMC}} \times R - F_{\mathrm{DMC}}/M_{\mathrm{DMC}} + 2 \times A_{\mathrm{DMO}} \times R - F_{\mathrm{DMO}}/M_{\mathrm{DMO}}) \times 100\%$$

$$\text{WTY of MF } (\mathrm{g\ kg_{cat}}^{-1}\ \mathrm{h}^{-1}) = \text{Mass of MF yield (g)}/(\text{Catalyst quality (kg)} \times \text{Time (h)})$$

$$\text{Mass activity } (\mathrm{mol\ g_{Pd}}^{-1}\ \mathrm{h}^{-1}) = \text{Mole of CO conversion (mol)}/(\text{Pd quality (g)} \times \text{Time (h)})$$

$[\mathrm{Ar}]_{\mathrm{in}}$ and $[\mathrm{Ar}]_{\mathrm{out}}$ are the concentrations of Ar at the inlet and outlet and $[\mathrm{CO}]_{\mathrm{in}}$ and $[\mathrm{CO}]_{\mathrm{out}}$ are the concentrations of CO at the inlet and outlet.

A_{DMM}, A_{MF}, A_{DMC} and A_{DMO} represent the peak areas of dimethoxymethane (DMM), methyl formate (MF), dimethyl carbonate (DMC) and dimethyl oxalate (DMO).

$R - F_{\mathrm{DMM}}$, $R - F_{\mathrm{MF}}$, $R - F_{\mathrm{DMC}}$ and $R - F_{\mathrm{DMO}}$ represent the relative correction factors of DMM, MF, DMC and DMO. The relative correction factor is calculated by standard sample injection.

M_{DMM}, M_{MF}, M_{DMC} and M_{DMO} represent the relative molecular mass of DMM, MF, DMC and DMO.

The selectivity of MF is calculated based on the MN reactant.

The mass activity is calculated based on the loading of noble metal Pd in the catalysts.

3. Results and discussion

3.1. Catalyst synthesis

The preparation process of the catalyst and a brief description of its structure are shown in Fig. 1. Following the aforementioned experimental procedure, three metal salts were added to the solution during the synthesis process. After calcination and nitric acid etching, the target catalyst was obtained. In this work, partial removal of Zn from the support was achieved *via* nitric acid etching, which induced local re-coordination and drove Pd migration into the generated vacancy sites. Subsequent calcination, following an anti-Ostwald ripening pathway, leveraged high-temperature reverse atomic migration and strong coordination interactions with the support surface to further convert Pd nanoparticles into atomically dispersed Pd single atoms.

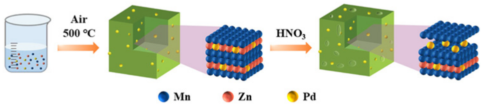

Fig. 1 Schematic illustration for the synthesis process and structural characteristics of Pd_1/ZMO.

3.2. Catalyst characterization

Powder information of the catalyst was acquired using XRD analysis, which was then compared to the standard card for $ZnMn_2O_4$ (PDF #9012842), confirming the successful synthesis of the desired catalyst. As shown in Fig. 2, the XRD powder test results of the Pd_1/ZMO catalyst before the reaction reveal no significant peaks corresponding to Pd clusters, and they align closely with the powder results of $ZnMn_2O_4$. This indicates that the introduction of Pd is minimal and does not affect the original lattice structure. Through etching followed by calcination, the high dispersion of Pd^{2+} within the spinel lattice was ensured. After 150 hours of reaction, the Pd_1/ZMO-150 catalyst still shows no detectable peaks for Pd, demonstrating the catalyst's high stability, as Pd does not easily form larger nanoparticles that could be detected. In addition, we also characterized the acidic sites of the catalyst by NH_3-TPD and py-FTIR, as shown in Fig. S1.[22,23]

As shown in Fig. 3a–f, SEM images reveal distinct differences in the surface morphology of the catalyst before and after nitric acid etching. In Fig. 3a and b, it is evident that the surface of the Pd_{NPs}/ZMO catalyst is relatively smooth prior to etching.[24] Conversely, in Fig. 3c and d, the Pd_1/ZMO catalyst obtained after etching and subsequent calcination exhibits numerous sheet-like structures on the spinel surface, contrasting sharply with the original smooth surface.[25] In Fig. 3e and f, the Pd_1/ZMO-150 catalyst still maintains the same sheet structure of the Pd_1/ZMO catalyst According to the BET analysis presented in Table S2, the

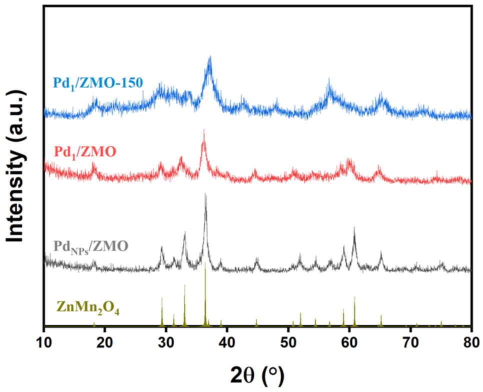

Fig. 2 XRD patterns of $ZnMn_2O_4$, Pd_{NP}/ZMO, Pd_1/ZMO, and Pd_1/ZMO-150 (after 150 hours of reaction).

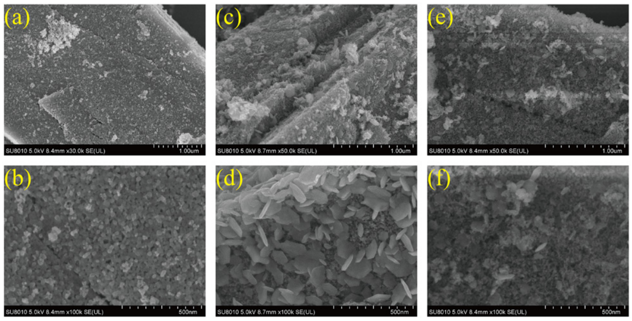

Fig. 3 SEM images of (a and b) Pd_{NP}/ZMO; (c and d) Pd_1/ZMO; (e and f) Pd_1/ZMO-150 after reaction.

specific surface area of the catalyst increased from 30.79 $m^2\ g^{-1}$ to 69.65 $m^2\ g^{-1}$ following the etching process, indicating a more pronounced defect structure on the spinel surface. The etched catalyst demonstrates a larger specific surface area and enhanced pore structure, which facilitates the adsorption of reactant gases at the active sites for catalytic reactions. Raman spectroscopy analysis of the catalyst, illustrated in Fig. S2a–S2c, shows characteristic peaks at 305 cm^{-1} and 316 cm^{-1} corresponding to the Mn–O_6 vibrations of the $ZnMn_2O_4$ spinel, while the peak at 664 cm^{-1} corresponds to Zn–O_4 vibration.[26] A decrease in the intensity of the Mn–O_6 peak, along with a redshift in its position post-etching, suggests an increased density of defects on the catalyst surface.[27]

During the catalyst synthesis, we employed diluted nitric acid treatment to etch a portion of the Zn^{2+} ions from the catalyst. Subsequent high-temperature treatment resulted in the formation of a heterostructure comprising $ZnMn_2O_4$@MnO_2. By controlling the etching time with diluted nitric acid, we could regulate the content of Zn^{2+} in the framework, thereby controlling the concentration of cation vacancies.[28] The subsequent calcination introduced oxygen vacancies at the zinc-deficient cation sites, facilitating the formation of MnO_2 with $Mn^{\delta+}$ and establishing electron transfer at the surface of the $ZnMn_2O_4$ spinel, resulting in the formation of the heterostructure.[29] As depicted in Fig. S3a and S3b, TEM images of Pd_{NP}/ZMO and Pd_1/ZMO reveal that the catalysts exhibit an elliptical, pebble-like morphology. Lattice spacing measurements indicate that the $ZnMn_2O_4$ (101) planes in Pd_1/ZMO are aligned with MnO_2 (111) planes, confirming the formation of a heterostructure on the surface following etching and calcination.

From Fig. 4a, the TEM image of the Pd_{NP} catalyst shows Pd nanoparticles, with a size of approximately 0.5 nm as measured. As shown in Fig. 4b, the AC-TEM of the Pd_1/ZMO catalyst can clearly observe the highly dispersed single-atom state of Pd on its surface. Fig. 4c shows the elemental mapping images of the Pd_1/ZMO catalyst, which shows that after etching and high-temperature treatment, Pd still exhibits high dispersion at a scale of 50 nm. As shown in Fig. S4, in the mapping diagram of the Pd_1/ZMO catalyst after 150 h reaction, Pd still maintains a high level of decentralization. It indicates that Pd_1 has good stability in the single-atom catalyst.[30]

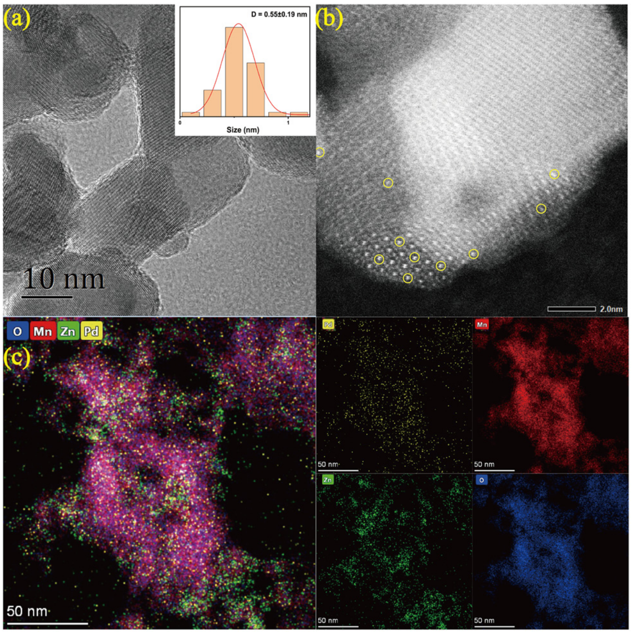

Fig. 4 (a) TEM image of Pd_{NPs}/ZMO; (b) AC-TEM image of Pd_1/ZMO; (c) mapping images of Pd_1/ZMO.

ICP elemental analysis, as presented in Table S1, determined the Pd loading in Pd_1/ZMO to be around 0.25 wt%. Following the etching with diluted nitric acid, a noticeable decrease in Zn content was observed. XPS analysis of the full elemental spectrum also indicated a significant reduction in the surface intensity of Zn.[31] Elemental mapping of Pd_1/ZMO further illustrated that some Zn^{2+} was etched away by the diluted nitric acid, while Mn was uniformly distributed both on the surface and within the catalyst, providing additional confirmation of the heterostructure's existence.[32]

Additionally, TOF-SIMS analysis in the negative ion mode, as illustrated in Fig. S6, S7 and Table S3, identifies a Pd–O–M signal, supporting the conclusion that Pd primarily exists as Pd^{2+} single atoms. The MnO_2 signal intensity on the catalyst surface is substantially higher than that of $ZnMn_2O_4$, indicating the formation of a $ZnMn_2O_4$@MnO_2 heterostructure post-etching. The presence of Pd–Zn and Pd–Mn bonds on the catalyst surface suggests that single-atom Pd is integrated within or bonded to the $ZnMn_2O_4$ lattice, contributing effectively as catalytic sites.[33]

Further XPS examination of Pd oxidation states, as shown in Fig. 5a and b, shows that Pd in Pd_{NP}/ZMO exists predominantly in the Pd^0 state, with both Pd nanoclusters.[27] In Pd_1/ZMO, Pd is solely in the Pd^{2+} form as Pd–O–M. As shown in the wide scan in Fig. S5a, the relative peak intensity of Zn 2p significantly decreases in Pd_1/ZMO after etching, indicating extensive Zn dissolution in dilute nitric acid, while the Pd 3d peak intensity remains largely unchanged, aligning

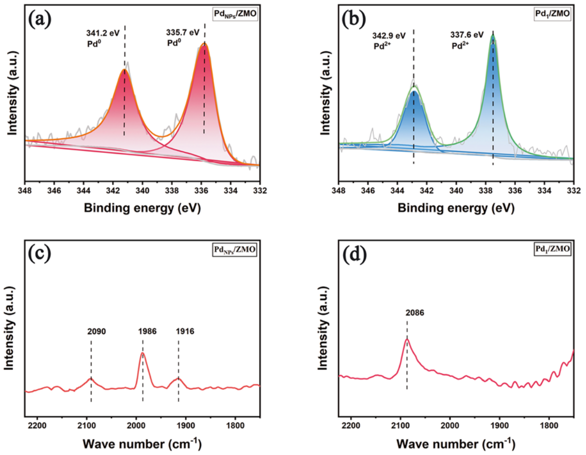

Fig. 5 XPS spectra of Pd 3d of (a) Pd_{NPs}/ZMO and (b) Pd_1/ZMO; the *in situ* CO-DRIFTS of (c) Pd_{NPs}/ZMO and (d) Pd_1/ZMO.

with expectations. Fitting analysis for the Mn elements, as presented in Fig. S5b and S5c, reveals Mn in the +2, +3, and +4 oxidation states within Pd_1/ZMO post-etching, suggesting the formation of a $ZnMn_2O_4$@MnO_2 heterostructure upon re-calcination.[34] SEM characterization confirms increased surface roughness and the presence of flaky structures after etching, indicative of MnO_2 nanosheets on the catalyst surface. After 150 hours, the Pd 3d XPS spectra reveal the coexistence of Pd^0 and Pd^{2+} species, indicating a dynamic valence state during the reaction (Fig. S11). Under the CO and H_2 atmosphere, Pd^{2+} is partially reduced to the Pd^0 state, whereas the MN containing reactive gas oxidizes Pd^0 back to Pd^{2+}. The absence of Pd clusters after 150 hours demonstrates that this redox cycling maintains an active electronic equilibrium around each Pd atom, thereby preserving its atomically dispersed state and ensuring stable catalytic performance.

XPS analysis of the oxygen element in the catalyst, as depicted in Fig. S5d and S5e, reveals that Pd_1/ZMO, post-etching, exhibits a greater abundance of lattice oxygen and adsorbed oxygen peaks compared to Pd_{NP}/ZMO. The more pronounced O_{ads} peak in Pd_1/ZMO can be attributed to the formation of cationic vacancies from the etching of Zn^{2+}, which, after calcination, introduces additional oxygen coordination. Additionally, Pd_1/ZMO has a larger specific surface area and porosity than Pd_{NP}/ZMO, which facilitates the exposure of Pd^{2+} single atoms on reactive surfaces. This exposure promotes CO adsorption and activation, enhancing further reactions with MN. Additionally, EPR measurements, as depicted in Fig. S8a, present a sinusoidal pattern in the *G*-value graph, with the *g* value determined to be 2.009, confirming the presence of oxygen vacancies.[35] Oxygen vacancies act as robust anchoring sites for individual Pd atoms, thereby inhibiting their surface diffusion and agglomeration under the reaction conditions. This is evidenced by the atomically dispersed Pd signals observed in HAADF-STEM images. Furthermore, these vacancies modulate the electronic structure of Pd and its adsorption properties.

The *in situ* CO-DRIFTS studies, as shown in Fig. 5c and d, reveal that peaks in the 1800–2000 cm^{-1} range correspond to bridge-type adsorption of CO on Pd, while those between 2000 cm^{-1} and 2100 cm^{-1} are attributed to linear adsorption on Pd. Peaks above 2100 cm^{-1} is attributed to the linear adsorption or multiple adsorptions of Pd in the high energy state. The peak observed near 2200 cm^{-1} corresponds to gaseous CO and was minimized by continuously purging with N_2 during the measurement to reduce interference from gas-phase species. For the Pd_{NP}/ZMO catalyst, prominent bridged CO adsorption bands appear at approximately 1916 cm^{-1} and 1986 cm^{-1}, indicating that bridge-type adsorption dominates on Pd nanoparticles. Additionally, a weaker band at 2090 cm^{-1} is assigned to linearly adsorbed CO, suggesting that a small portion of Pd exists as isolated single sites in Pd_{NP}/ZMO. In contrast, the Pd_1/ZMO catalyst exhibits only a single linear CO adsorption band at 2086 cm^{-1}, confirming that Pd is exclusively present in a highly dispersed single-atom configuration.[36]

3.3. Catalyst performance

The catalytic performance was evaluated, with the results illustrated in Fig. 6a and b. Based on the above catalyst evaluation conditions, we conduct evaluation tests on the performance and lifespan of the catalyst. A comparison between the Pd/α-Al_2O_3, Pd_{NP}/ZMO and Pd_1/ZMO catalysts was conducted. Firstly, 1 wt% loading of Pd_{NP}/α-Al_2O_3 exhibited good conversion and selectivity, while the 0.25 wt% Pd_{NP}/ZMO catalyst only exposed a limited number of active Pd sites, resulting in relatively low CO conversion and poor selectivity. In contrast, the Pd_1/ZMO catalyst with the same 0.25 wt% loading exhibited the highest CO conversion and excellent MF selectivity, as well as highly stable catalytic performance with a CO conversion to 64% and MF selectivity to 96%. The mass activity of Pd_{NP}/α-Al_2O_3 is 2.3 mol g_{Pd}^{-1} h^{-1} and mass activity of Pd_1/ZMO is 9.1 mol g_{Pd}^{-1} h^{-1}. The mass activity of Pd_1/ZMO is about four times that of Pd_{NP}/α-Al_2O_3. In addition, it maintains stable operation for 150 hours without any decrease in performance, demonstrating excellent durability. Under the same loading capacity of Pd, the performance of the single-atom catalyst is superior to that of the nano-catalyst.

3.4. Mechanism speculation

The reaction between CO and MN typically involves the formation of three main products: MF, DMC, and DMO. While

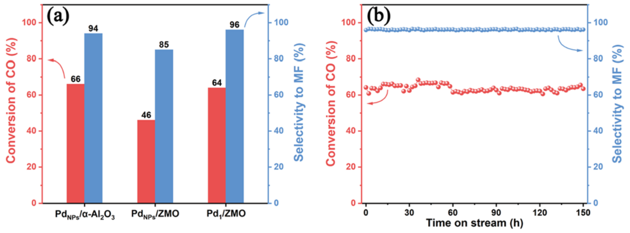

Fig. 6 (a) Catalyst performance comparison diagram; (b) 150-hour reaction performance diagram of Pd_1/ZMO.

the mechanisms of DMC and DMO formation have been widely discussed, with a general academic consensus that the formation of DMC primarily follows the Eley–Rideal mechanism (E–R mechanism) and DMO follows the Langmuir–Hinshelwood mechanism (L–H mechanism), the mechanism for MF formation has been less explored. This paper investigates and reasonably hypothesizes the mechanism for MF formation in a CO, MN, and H_2 reaction system.[37]

The catalyst active metal is Pd. During the CO esterification reaction to generate MF, Pd interacts with various reactant gases, leading to the formation of different intermediates, which subsequently react to form the final product MF. The overall three-component reaction is as follows:

$$2CH_3ONO + 2CO + H_2 \rightarrow 2HCOOCH_3 + 2NO$$

In this reaction system, the primary processes involve the coupling cleavage of Pd and MN, generating the Pd–OCH_3 intermediate. Pd also adsorbs CO, forming Pd–CO, and these intermediates can further generate Pd–$COOCH_3$, a crucial intermediate in CO esterification. Additionally, H_2 interacts with Pd, forming Pd–H through homolytic cleavage.

$$^*OCH_3 + {^*CO} \rightarrow {^*COOCH_3}$$

$$^*COOCH_3 + \cdot H \rightarrow HCOOCH_3$$

To validate this hypothesis, a series of characterization experiments were performed. First, *in situ* CO-DRIFTS tests were conducted. As seen in Fig. 5c and d, both Pd_{NP}/ZMO and Pd_1/ZMO adsorb CO. However, due to better dispersion, Pd_1/ZMO prefers linear adsorption, while Pd_{NP}/ZMO shows bridge adsorption. While both adsorb CO, this single characterization does not provide a conclusive explanation. Thus, *in situ* CO-MN DRIFTS characterization was also conducted. As shown in Fig. 7a, b and S9, the peaks at 1739 and 1192 cm^{-1} are ascribed to the C═O and C–O stretching vibrations of adsorbed $^*COOCH_3$ intermediates. Moreover, the peak at 1444 cm^{-1} is assigned to the C–H deformation of adsorbed $^*COOCH_3$ intermediates on the catalyst surface. Strong new peaks appear at 1765 and 1269 and 1297 cm^{-1} with the passing of time, which are ascribed to the C═O and C–O stretching vibrations of gaseous MF product, respectively. Meanwhile, the peaks appeared at 1901 and 1843 cm^{-1} are assigned to the bimodal peaks of gaseous NO, indicating that NO was also produced during the reaction. Additionally, the peak at 2960 cm^{-1} is assigned to the C–H stretching vibration of the methyl group.

For our reaction system, which involves H_2, the formation of MF is more likely to proceed *via* the L–H mechanism, which has a lower reaction barrier. The process is as follows: Pd adsorbs CO linearly, forming Pd–CO. MN adsorbs and dissociates on Pd, forming free radicals that bond with Pd to form Pd–OCH_3. Pd–OCH_3 couples with Pd–CO and undergoes electron transfer to form Pd–$COOCH_3$. The introduction of H_2 leads to its dissociation into ·H free radicals under Pd influence. Some of these ·H free radicals bond with Pd to form Pd–H. Pd–$COOCH_3$ and Pd–H undergo coupling to form MF.

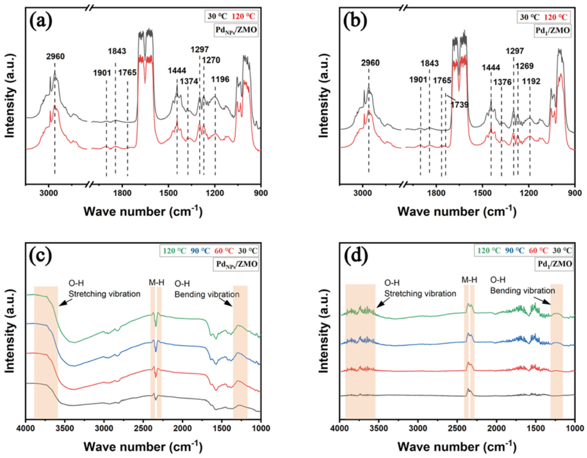

Fig. 7 The *in situ* CO-MN DRIFTS of (a) Pd_{NP}/ZMO and (b) Pd_1/ZMO; the *in situ* H_2-DRIFTS of (c) Pd_{NP}/ZMO and (d) Pd_1/ZMO.

According to reports, the rate-determining steps in the formation of DMC, DMO and MF are different. For MF, the key rate-determining step is the coupling reaction between Pd–H and Pd–$COOCH_3$ during the hydrogenation step of the experimental reaction.[38]

$$^*COOCH_3 + \cdot H \rightarrow HCOOCH_3$$

To further investigate this mechanism, *in situ* monitoring was performed in a 3% H_2 atmosphere. As seen in Fig. 7c and d, clear differences between Pd_{NP}/ZMO and Pd_1/ZMO catalysts can be observed. Pd_1/ZMO shows a more pronounced M–H bond vibration peak due to stronger interaction with H_2. In contrast, Pd_{NP}/ZMO shows a weaker M–H bond peak, indicating weaker adsorption of H_2 and consequently lower catalytic activity in the reaction.[39–41]

It is difficult to directly observe the ·H free radicals from H_2. Therefore, free radical scavengers such as 5,5-dimethyl-1-pyrroline *N*-oxide (DMPO) were added to the test to capture them for testing. The *in situ* H_2-EPR characterization was carried out to observe the interaction mechanism between the active metal Pd and H_2. As shown in Fig. S8b, the intensity of hydrogen free radical peaks was compared. It is clear that, compared to catalysts with active Pd, the $ZnMn_2O_4$ support generates some free radicals, but their intensity is weaker. The overall peak shape and peak area ratio prove the presence of hydrogen free radicals and multiple equivalent hydrogen atoms coupled together.[42,43] Additionally, considering that the support contains metals such as Zn and Mn that can adsorb and partially activate H_2 to form hydrogen free radicals, the EPR spectra for Pd_{NP}/ZMO and Pd_1/ZMO show little difference in peak shape, position, and intensity. However, based on previous *in situ* H_2-DRIFTS analysis, Pd_{NPs} can generate ·H free radicals but with a weaker M–H peak, indirectly indicating that the generated ·H

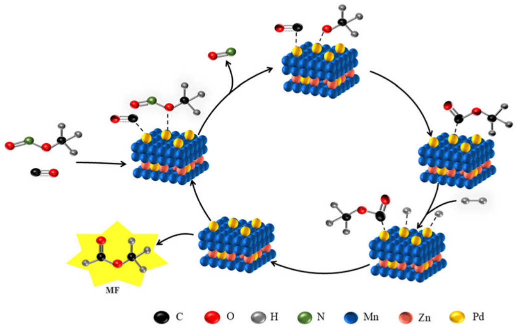

Fig. 8 The proposed catalytic mechanism of CO esterification to MF.

free radicals do not extensively interact with the active Pd, resulting in lower reaction activity. In contrast, Pd_1 single atoms not only generate ·H free radicals but also facilitate their bonding with Pd to form Pd–H bonds, thus promoting the coupling with Pd–$COOCH_3$ to form MF.

In summary, this study, through systematic experimental and theoretical analysis, provides an in-depth understanding of the mechanism by which single-atom catalysts catalyze the CO esterification to generate MF, as shown in Fig. 8. To further elucidate the reaction mechanism of CO esterification to methyl formate, we carried out DFT calculations and constructed a detailed energy profile (Fig. S12). The analysis reveals that the hydrogenation step requires the highest energy input among all elementary steps, indicating that it is the rate-determining step. Our results show that loading single-atom Pd onto a $ZnMn_2O_4$ support significantly lowers the activation energy of the reaction and facilitates the dissociation of H_2 at the active sites, leading to the generation of highly active ·H free radicals. These ·H free radicals further couple with reaction intermediates, driving the overall reaction forward. The EPR and *in situ* DRIFTS data consistently support this mechanistic model. Future studies will focus on exploring the impact of the reaction conditions and catalyst structural adjustments on the mechanism to achieve more efficient and stable catalytic conversion processes.

Conclusions

In summary, the Pd_1/ZMO single-atom catalyst was synthesized for CO esterification to MF, significantly reducing the noble metal Pd loading and exhibiting 4 times the mass activity of Pd_{NP}/ZMO catalysts. By analysing the structure of the single-atom catalyst, the reasons for its high activity and stability in the reaction were revealed. And the formation of heterostructures in the carrier enhances the MSI between the embedded Pd single atoms and the carrier. Meanwhile, the reaction intermediates were characterized by *in situ* DRIFTS, and the whole reaction steps were reasonably speculated. A reasonable reaction pathway for the CO esterification to MF was proposed. In heterogeneous catalysis, single atom catalysts exhibit significant advantages. And this work can provide new ideas for the reduction of noble metals in catalysts, and has important guiding significance for improving metal utilization and reducing noble metal loading.

Author contributions

Xiao-Long Wang: writing – original draft, investigation, and formal analysis. Xiao-Yuan Tan: formal analysis and data curation. Jian Lin: investigation and data curation. Hua Wang: investigation and data curation. Jing Sun: methodology and data curation. Zhong-Ning Xu: funding acquisition, writing – review & editing, supervision. Guo-Cong Guo: conceptualization, funding acquisition, and supervision.

Conflicts of interest

There are no conflicts to declare.

Data availability

Supplementary information: NH_3-TPD, Raman, TEM, Mapping, XPS, TOF-SIMS, EPR, *In situ* DRIFTS, ICP, BET, and Mass-to-charge ratio data are available in the SI. See DOI: **https://doi.org/10.1039/D5CY00841G**.

The authors confirm that the data supporting the findings of this study are available within the article and its SI.

Acknowledgements

This work was supported by the Strategic Priority Research Program of the Chinese Academy of Sciences (XDA29030600), the National Natural Science Foundation of China (22172171), the Joint Fund of Yulin University and Dalian National Laboratory for Clean Energy (Grant. YLU-DNL Fund 2022010), and the Self-deployment Project Research Program of Haixi Institutes (CXZX-2022-GH05).

Notes and references

1 W. Zhou, K. Cheng, J. Kang, C. Zhou, V. Subramanian, Q. Zhang and Y. Wang, *Chem. Soc. Rev.*, 2019, **48**, 3193–3228.
2 G. Jenner, *Appl. Catal., A*, 1995, **121**, 25–44.
3 R. Sang, Z. Wei, Y. Hu, E. Alberico, D. Wei, X. Tian, P. Ryabchuk, A. Spannenberg, R. Razzaq, R. Jackstell, J. Massa, P. Sponholz, H. Jiao, H. Junge and M. Beller, *Nat. Catal.*, 2023, **6**, 543–550.
4 M. Ai, *J. Catal.*, 1982, **77**, 279–288.
5 D. Kaiser, L. Beckmann, J. Walter and M. Bertau, *Catalysts*, 2021, **11**, 869.
6 L. He, H. Liu, C. Xiao and Y. Kou, *Green Chem.*, 2008, **10**, 619.
7 H. Zhao, M. Lin, K. Fang, J. Zhou and Y. Sun, *Appl. Catal., A*, 2016, **514**, 276–283.
8 A. Wittstock, V. Zielasek, J. Biener, C. M. Friend and M. Bäumer, *Science*, 2010, **327**, 319–322.
9 L. Rong, Z. Xu, J. Sun and G. Guo, *J. Energy Chem.*, 2018, **27**, 238–242.
10 L. Sun, J. Xu, X. Liu, B. Qiao, L. Li, Y. Ren, Q. Wan, J. Lin, S. Lin, X. Wang, H. Guo and T. Zhang, *ACS Catal.*, 2021, **11**, 5942–5950.

11 S. Cao, M. Yang, A. O. Elnabawy, A. Trimpalis, S. Li, C. Wang, F. Göltl, Z. Chen, J. Liu, J. Shan, M. Li, T. Haas, K. W. Chapman, S. Lee, L. F. Allard, M. Mavrikakis and M. Flytzani-Stephanopoulos, *Nat. Chem.*, 2019, **11**, 1098–1105.

12 Y. Wu, Y. Tong, Y. Luo, J. Xu, X.-K. Gu and M. Ding, *ACS Catal.*, 2024, 15869–15878.

13 Q. Wang, D. Zhang, Y. Chen, W.-F. Fu and X.-J. Lv, *ACS Sustainable Chem. Eng.*, 2019, **7**, 6430–6443.

14 L. Xiong, H. Qi, S. Zhang, L. Zhang, X. Liu, A. Wang and J. Tang, *Adv. Mater.*, 2023, **35**, 2209646.

15 L. Chen, Z. Qi, X. Peng, J.-L. Chen, C.-W. Pao, X. Zhang, C. Dun, M. Young, D. Prendergast, J. J. Urban, J. Guo, G. A. Somorjai and J. Su, *J. Am. Chem. Soc.*, 2021, **143**, 12074–12081.

16 Z. Wei, *Sci. China: Chem.*, 2022, **65**, 421–422.

17 H. Zhang, S. Fang and Y. H. Hu, *Catal. Rev.: Sci. Eng.*, 2022, **64**, 491–532.

18 A. O. Ibrahim, A. Halilu, W. M. A. W. Daud, M. F. AbdulPatah and J. C. Juan, *Mol. Catal.*, 2022, **529**, 112535.

19 L. Li, Q. Yang, D. Wang, Y. Peng, J. Yan, J. Li and J. Crittenden, *Chem. Eng. J.*, 2021, **421**, 127828.

20 K. Liu, X. Zhao, G. Ren, T. Yang, Y. Ren, A. F. Lee, Y. Su, X. Pan, J. Zhang, Z. Chen, J. Yang, X. Liu, T. Zhou, W. Xi, J. Luo, C. Zeng, H. Matsumoto, W. Liu, Q. Jiang, K. Wilson, A. Wang, B. Qiao, W. Li and T. Zhang, *Nat. Commun.*, 2020, **11**, 1263.

21 X. I. Pereira-Hernández, A. DeLaRiva, V. Muravev, D. Kunwar, H. Xiong, B. Sudduth, M. Engelhard, L. Kovarik, E. J. M. Hensen, Y. Wang and A. K. Datye, *Nat. Commun.*, 2019, **10**, 1358.

22 Y.-P. Xu, Z.-Q. Wang, H.-Z. Tan, K.-Q. Jing, Z.-N. Xu and G.-C. Guo, *Catal. Sci. Technol.*, 2020, **10**, 1699–1707.

23 G. Kumar, L. Ren, Y. Pang, X. Li, H. Chen, J. Gulbinski, P. J. Dauenhauer, M. Tsapatsis and O. A. Abdelrahman, *ACS Catal.*, 2021, **11**, 9933–9948.

24 G. Huo, X.-W. Wang, Z.-B. Zhang, Z. Song, X.-M. Kang, M.-X. Chen, Q. Wang, X.-Z. Fu and J.-L. Luo, *J. Energy Chem.*, 2020, **51**, 81–89.

25 B. Wang, Q. Yang, B. Li, H. Ma, Y. Xuan, C. Gao, Y. Liang, K. Zhang, Q. Chang, O. Broesicke, H. Wang, D. Wang, T. Luan, K. Han, C. Lu and J. Crittenden, *Appl. Catal., B*, 2023, **332**, 122753.

26 Y. Zhang, P. Zhang, Y. Xu, X. Song, H. Wang and T. Ma, *J. Mater.*, 2021, **7**, 699–707.

27 R. Chen, Z. Wang, S. Chen, W. Wu, Y. Zhu, J. Zhong and N. Cheng, *ACS Energy Lett.*, 2023, **8**, 3504–3511.

28 S. Mallick, V. S. K. Choutipalli, S. Bag, V. Subramanian and C. R. Raj, *ACS Appl. Mater. Interfaces*, 2022, **14**, 37577–37586.

29 Y. Aponte and H. De Lasa, *Ind. Eng. Chem. Res.*, 2017, **56**, 1948–1960.

30 S. Ding, H.-A. Chen, O. Mekasuwandumrong, M. J. Hülsey, X. Fu, Q. He, J. Panpranot, C.-M. Yang and N. Yan, *Appl. Catal., B*, 2021, **281**, 119471.

31 Y. Xiang, P. Ju, Y. Wang, Y. Sun, D. Zhang and J. Yu, *Chem. Eng. J.*, 2016, **288**, 264–275.

32 K. Jiang, W. Huang, T. Song, P. Wu, W. Wang, Q. Chen, M. Wang and G. Guo, *Adv. Funct. Mater.*, 2023, **33**, 2304351.

33 B. Bai, Y. Ye, F. Jiao, J. Xiao, Y. Pan, Z. Cai, M. Chen, X. Pan and X. Bao, *J. Am. Chem. Soc.*, 2024, **146**, 34909–34915.

34 H. Tian, L. Zeng, Y. Huang, Z. Ma, G. Meng, L. Peng, C. Chen, X. Cui and J. Shi, *Nano-Micro Lett.*, 2020, **12**, 161.

35 S. Wu, X. Liu, X. Lian, G. Tian, C. Janiak, Y. Zhang, Y. Lu, H. Yu, J. Hu, H. Wei, H. Zhao, G. Chang, G. Van Tendeloo, L. Wang, X. Yang and B. Su, *Adv. Mater.*, 2018, **30**, 1802173.

36 Z.-N. Xu, J. Sun, C.-S. Lin, X.-M. Jiang, Q.-S. Chen, S.-Y. Peng, M.-S. Wang and G.-C. Guo, *ACS Catal.*, 2013, **3**, 118–122.

37 Z.-Y. Chi, L.-Q.-Q. Yang, X.-G. Li, Y.-L. He and W.-D. Xiao, *Chem. Eng. J.*, 2022, **446**, 136656.

38 Q. Li, Z. Zhou, R. Chen, B. Sun, L. Qiao, Y. Yao and K. Wu, *Phys. Chem. Chem. Phys.*, 2015, **17**, 9126–9134.

39 Y. A. Agafonov and A. I. Serykh, *Mol. Catal.*, 2024, **559**, 114104.

40 F. Haque, F. Finocchi, S. Chenot, J. Jupille and S. Stankic, *J. Phys. Chem. C*, 2021, **125**, 25841–25850.

41 Z. Chen, P. Yuan, C. Chen, X. Wang, J. Wang, J. Jia, B. Davaasuren, Z. Lai, N. M. Khashab, K. Huang, O. M. Bakr, J. Yin and K. N. Salama, *Adv. Mater.*, 2024, **36**, 2404291.

42 L. Qin, L. Yang, J. Yang, R. Weber, K. Ranguelova, X. Liu, B. Lin, C. Li, M. Zheng and G. Liu, *iScience*, 2021, **24**, 102193.

43 S. Okazaki and K. Takeshita, *Appl. Magn. Reson.*, 2018, **49**, 881–892.